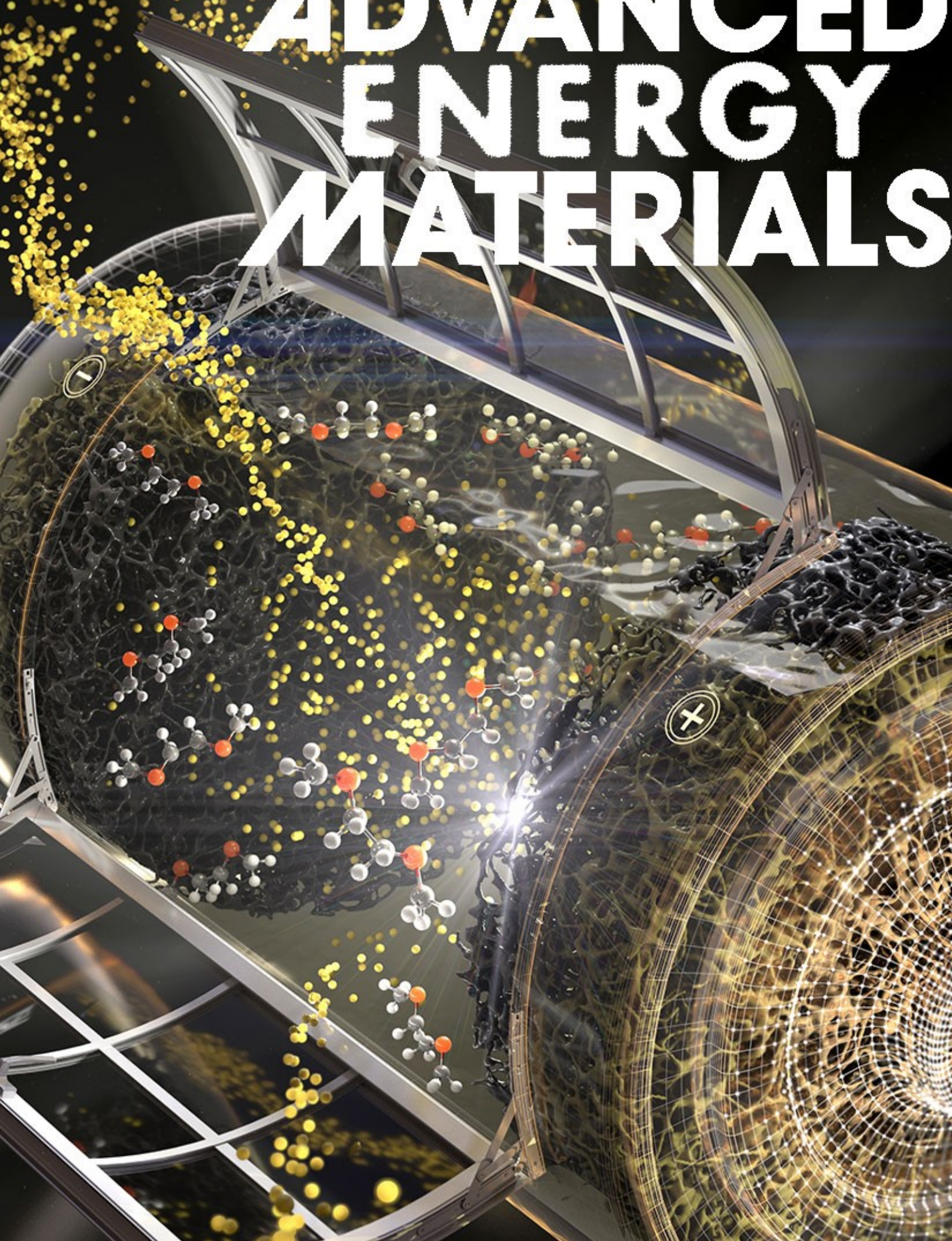


ADVANCED ENERGY MATERIALS



Relationship between Multivalent Cation Charge Carriers and Organic Solvents on Nanoporous Carbons in 4 V-Window Magnesium Ion Supercapacitors

Seongbak Moon, Sang Moon Lee, Hyung-Kyu Lim,* Hyoung-Joon Jin,* and Young Soo Yun*

Multivalent charge carriers with a smaller ionic radius exhibit strong ionic interactions with solvent molecules. This can lead to unusual characteristics that typically are not observed in conventional monovalent charge carriers. Herein, the capacitive Mg ion storage behavior on nanoporous carbons is investigated within different solvent systems. A larger multivalent charge carrier, Ca ions, and alkali cations with different ionic radii are used as a comparison. In addition, the effects of nanopores on solvated Mg ion physisorption are observed in two types of nanoporous carbon, namely typical microporous carbon and ultramicrosoporous carbon (MEC). The oxidation stability of dimethoxyethane (DME) solvent is significantly improved by forming a solvation complex with Mg ions, while the destabilization effect of DME induced by anions is suppressed by the Mg ion charge carriers. The use of MEC as an active electrode material in a Mg ion-DME electrolyte system leads to high electrochemical performance of the Mg ion supercapacitor over a wide range of operating voltages. A high-performance 4 V Mg ion supercapacitor with charge-injected symmetric MEC-based electrodes is evaluated, where excellent specific energy and power densities of $\approx 106 \text{ W h kg}^{-1}$ and $\approx 11870 \text{ W kg}^{-1}$, respectively, are achieved.

charge storage mechanism differs greatly from conventional non-polarized faradic electrodes that operate based on chemical potential.^[4] Physisorption is a very rapid and reversible process, thereby facilitating high power capabilities and a good long-term cycle life.^[5,6] However, the relatively small charge capacity of supercapacitors is regarded as a critical limitation for practical application.^[1,3,6]

Physisorption capacitance is proportional to the electrochemically active surface area, and inversely proportional to the distance between the IPE and charge carrier. This relationship may be expressed as:

$$C = \epsilon_r \epsilon_0 A / d \quad (1)$$

where C is the capacitance, ϵ_r is the electrolyte dielectric constant, ϵ_0 is vacuum permittivity, A is the electrochemically active surface area, and d is the charge separation distance (the Debye length).^[1,3]

Hence, most of the previous studies on supercapacitors have concentrated on two major issues, the development of high surface area IPEs, and the fabrication of well-fitted pore structures based on optimized electrode material properties.^[7–18] This research has demonstrated that nanoporous carbon with a high specific surface area and a well-developed nanoporous or sub-nanoporous structure are optimal IPE materials for supercapacitors. However, the charge storage performance of

1. Introduction

Supercapacitors are widely used energy storage devices, and are composed of an ideally polarized electrode (IPE) pair and ionic charge carriers dissolved in a solvent system.^[1] Under an electric field, the charge carriers stabilized by the solvent molecules become polarized and accumulate on the surface of the IPEs to form electrochemical double layers (EDL).^[2,3] This

S. Moon, Prof. H.-J. Jin
Program in Environmental and Polymer Engineering
Inha University
100, Inha-ro, Michuhol-gu, Incheon 22212, South Korea
E-mail: hjjin@inha.ac.kr


Dr. S. M. Lee
Research Center for Materials Analysis
Korea Basic Science Institute (KBSI)
169-148, Gwahak-ro, Yuseong-gu, Daejeon 34133, South Korea

Prof. H.-K. Lim
Division of Chemical Engineering and Bioengineering
Kangwon National University
Chuncheon, Gangwon-do 24341, South Korea
E-mail: hklim@kangwon.ac.kr

Prof. H.-J. Jin
Department of Polymer Science and Engineering
Inha University
E-mail: 100, Inha-ro, Michuhol-gu, Incheon 22212, South Korea

Prof. Y. S. Yun
KU-KIST Graduate School of Converging Science and Technology
Korea University
145, Anam-ro, Seongbuk-gu, Seoul 02841, South Korea
E-mail: c-ysyun@korea.ac.kr

Prof. Y. S. Yun
Department of Integrative Energy Engineering
Korea University
145, Anam-ro, Seongbuk-gu, Seoul 02841, South Korea

 The ORCID identification number(s) for the author(s) of this article can be found under <https://doi.org/10.1002/aenm.202101054>.

DOI: 10.1002/aenm.202101054

nanoporous carbons has been primarily investigated under monovalent charge carriers.^[7–18] Despite these advances in the understanding of monovalent ion-based supercapacitors, insights regarding multivalent ion storage behaviors, especially on nanoporous carbons, remain grossly inadequate.

Multivalent ions with a smaller ionic radius (e.g., Mg ions) have a significant influence on solvent molecules via strong ionic interactions with solvation sheaths and coordination solvent molecules.^[19,20] This can affect the EDL configuration, as well as the oxidation and reduction potentials of the electrolyte system. Moreover, the Debye lengths of multivalent ions are longer than those of monovalent ions with a similar ionic radius.^[21] Debye length and ionic interaction are key factors in capacitive charge storage performance, particularly on nanopores, because EDL capacitance occurs within confined nanopores.^[9–13] In these cases, a limited number of charge carriers can be inserted within the superionic state nanopores.^[22] However, the ionic behavior associated with multivalent charge carriers is highly dependent on the type of specific ions, solvent molecules, and nanopores.^[19–21,23] This complex relationship has limited research progress regarding energy storage systems based on multivalent ion charge carriers. Thus, a systematic study is required to offer a deeper understanding.

This study aimed to evaluate the capacitive Mg ion storage behavior on nanoporous carbons in diverse organic solvents, such as dimethoxyethane (DME), acetonitrile (ACN), dimethyl carbonate (DMC), and propylene carbonate (PC). Larger multivalent ions, namely calcium ions, and alkali ions with different ionic radii were evaluated under the same electrochemical conditions to serve as a comparison. Different nanoporous carbon structures, ultra-mesoporous carbon (MEC) and microporous carbon (MIC) structures, were evaluated to provide an insight into the effects of pore size. These systematic studies revealed that capacitive charge storage behavior is highly dependent on charge carrier, solvent, and pore structure of the electrode material. Most notably, a system based on the smaller multivalent Mg ion charge carrier and DME electrolyte exhibited a very wide and stable operating voltage window of >4 V due to the strong ionic interaction between Mg and DME.

2. Results and Discussion

Two different types of nanoporous carbon, MICs and MECs, were prepared from a polymer precursor via a one-step pyrolysis and chemical activation process using potassium hydroxide. The polymer to potassium hydroxide ratio played a key role in the formation of the contrasting nanoporous structures, where a ratio of 1:3 produced MEC and 1:1 produced MIC. The nitrogen adsorption and desorption isotherm curves of the MICs and MECs clearly confirmed the presence of distinct pore structures (Figure 1a). Specifically, the sudden increase in the isotherm curves within the low relative pressure region (<0.02) was attributed to monolayer adsorption on the open surfaces, where both samples exhibited similarly large nitrogen adsorption capacities of >400 cm³ g⁻¹. This was indicative of a high specific surface area. However, the subsequent linear increases in the isotherm curves differed between the two samples, which were indicative of different pore structures. The linearly

increasing section of the isotherm curve for the MECs covered a larger relative pressure region (≈ 0.5), which is typical for ultramesoporous structures with pores of a few nanometers in size.^[24] In contrast, the isotherm curve of the MICs was typical of an International Union of Pure and Applied Chemistry type-I microporous structure. The pore size distribution data further confirmed that the MICs and MECs had different pore structures (Figure 1b). Specifically, the MICs had a peak pore volume at ≈ 2 nm pore in width, where most pores were <2 nm, while the MECs had a larger pore width mainly distributed between 2 and 5 nm. The pore size distributions of the MICs and MECs were also characterized by using the non-local density functional theory (DFT) method (Figure S1, Supporting Information). The larger pore width of the MECs could also be clearly confirmed in the non-local DFT model, supporting their difference in pore structure. The Brunauer–Emmett–Teller (BET) surface area of the MECs was ≈ 3300 m² g⁻¹, where the surface area associated with the micropores (<2 nm) was only 190 m² g⁻¹, and the mesopores accounted for the remaining 3110 m² g⁻¹. In contrast, the MICs had a micropore surface area of 1800 m² g⁻¹, which corresponded to over half of the total specific BET surface area (≈ 2950 m² g⁻¹).

Despite the stark differences in the pore structures of the two types of nanoporous carbon, the carbon microstructures were very similar. Specifically, the Raman spectra included overlapped and broad peaks at ≈ 1322 and ≈ 1578 cm⁻¹, which originated from the A_{1g} and E_{2g} vibration modes of poly hexagonal carbon rings, respectively (Figure 1c).^[25] The E_{2g} vibration mode, referred to as the G band, indicated that the carbon building blocks included a well-ordered six-membered carbon structure. In contrast, the A_{1g} breathing mode, referred to as the D band, was indicative of a disordered sp² carbon structure. Further, the high intensity of the D band was related to a large number of sp³ carbon defects within the carbon structure. These topological defects deformed the aromatic carbon plane permanently, leading to poorly stacked graphitic lattices with higher *d*-spacing. Chemical activation reagents, such as potassium hydroxide, attack the carbon building blocks synthesized during pyrolysis, thereby generating a highly expanded and disordered carbon structure. The nanopores of the MICs and MECs originated from open spaces between the highly expanded carbon lattices, where the wider nanopores indicated that a more loosely packed carbon structure was formed during the harsh activation process. In the first-ordered region (1100–1800 cm⁻¹), the Raman spectra were further specifically deconvoluted as five distinctive peaks because additional smaller bands associated to disordered carbon structures appear at a frequency of ≈ 1100 , ≈ 1500 , and ≈ 1620 cm⁻¹. The peaks at ≈ 1100 and ≈ 1500 cm⁻¹ are related with amorphous sp² carbons and residual sp³ carbons, respectively. And the D' peak at ≈ 1620 cm⁻¹ appears whenever D band is observed.^[26] In the deconvoluted Raman spectra, the D to G intensity ratio (I_D/I_G) was used to calculate the lateral size (L_a) of the ordered domain in the carbon building blocks based on the Tuinstra and Koenig equation (Figure S2, Supporting Information).^[27] Similar L_a values of ≈ 1.3 and ≈ 1.1 nm were calculated for the MICs and MECs, respectively. However, the lack of peaks in the XRD patterns throughout the entire 2θ range of 5° to 60° was indicative of poor stacking ordering of the carbon building

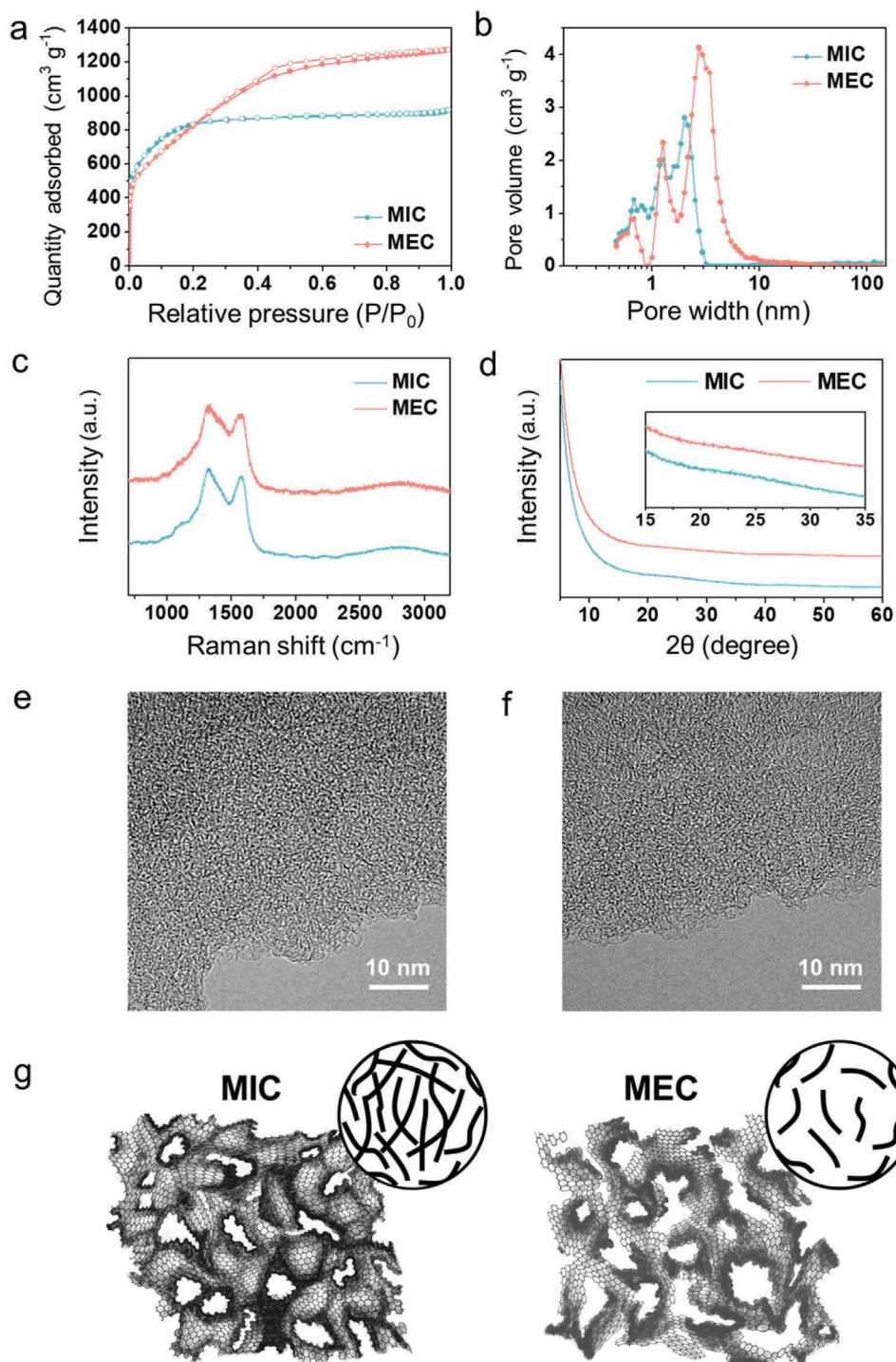


Figure 1. Materials properties of MICs and MECs. a) Nitrogen adsorption and desorption isotherm curves, b) pore size distribution data, c) Raman spectra, d) XRD patterns (Inset of the two theta region between 15 and 35°), high-resolution FE-TEM images of e) MIC and f) MEC, and g) schematic images showing carbon local microstructures of MIC and MEC.

blocks (Figure 1d). Further, the surge increase in the XRD patterns in the lower 2θ region was attributed to the presence of large amounts of nanopores.

High-resolution field emission transmission electron microscopy (FE-TEM) images of the MICs and MECs confirmed

their amorphous carbon structures with no long-range crystalline graphitic domains (Figure 1e,f). The nanoporous structures of the MICs and MECs were presented schematically to illustrate their subtle differences (Figure 1g). In addition, the surface chemical properties of the MICs and MECs were

analyzed using X-ray photoelectron spectroscopy (XPS, see Figure S3, Supporting Information). The carbon 1s spectra of both samples were related similar functional groups, such as C=C, C-C, C-O, and C=O bonding at 284.4, 285.1, 286.4, and 288.5 eV, respectively (Figure S3a, Supporting Information). The O 1s spectra revealed that the oxygen functional groups existed as two obvious configurations of either C=O or C-O bonds centered at 531.3 and 532.9 eV, respectively (Figure S3b, Supporting Information). According to the XPS results, the O/C ratios of the MICs and MECs were 0.10 and 0.11, respectively.

Overall, the characterization results confirmed that the MICs and MECs had similar material properties, with the exception

of their different nanoporous structures. Therefore, these nanoporous samples could be used as electrode materials to examine the effects of pore size on capacitive charge storage behaviors via electrochemical analysis.

Electrochemical analysis was conducted in a coin cell comprising either MIC- or MEC-based working electrodes, a porous glass fiber separator, and a MEC counter electrode with an active mass loading ≈ 20 times larger than that of the working electrode. The symmetric electrode configuration was based on a large gap in active mass loading contents, thus voltage changes mainly occurred in the working electrode (Figures S4 and S5, Supporting Information). This allowed for

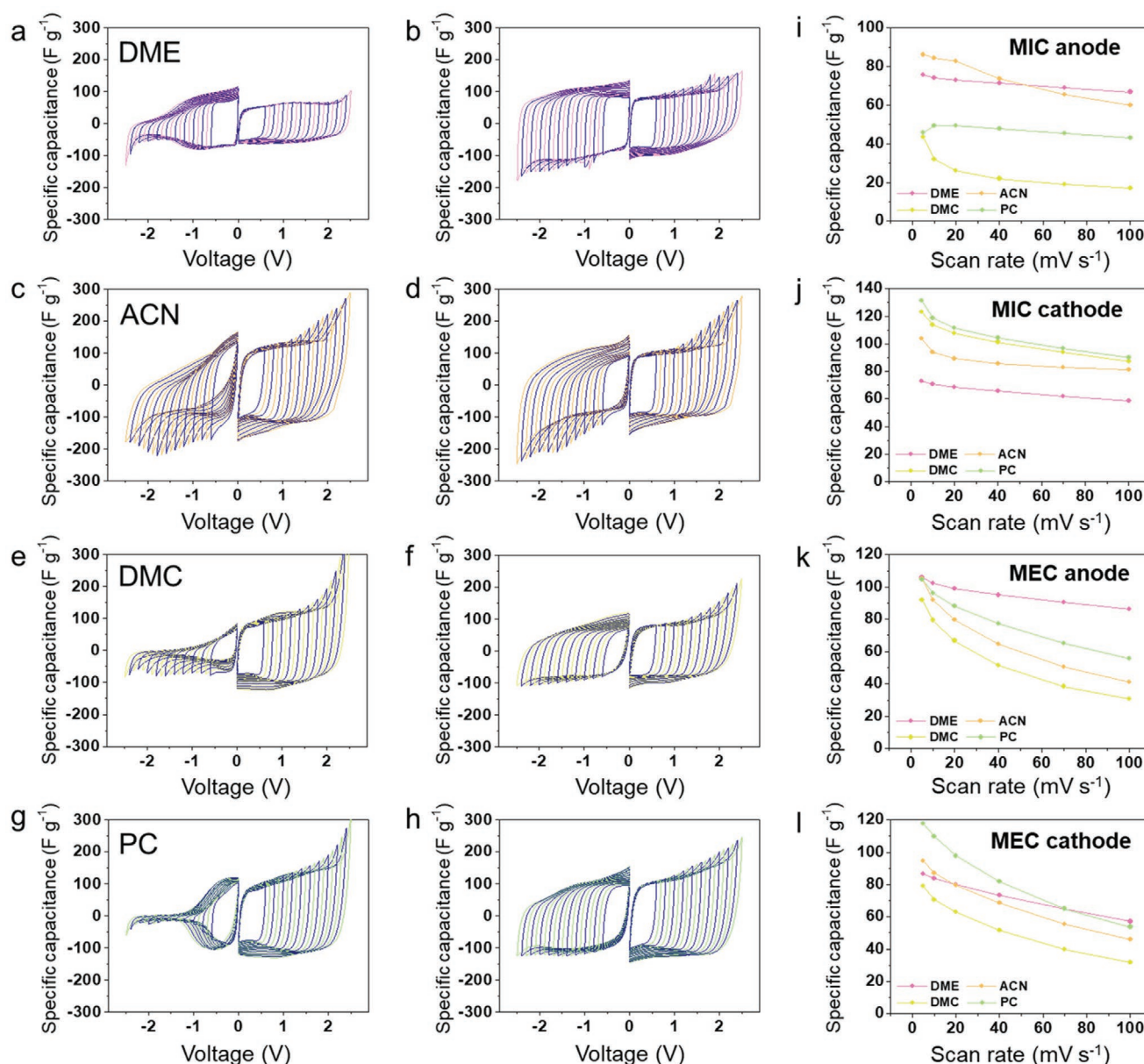


Figure 2. Mg ion storage behaviors of MIC and MEC electrodes under different organic solvent systems at different operating voltage windows. Cyclic voltammograms of MIC electrodes in a) DME, c) ACN, e) DMC and g) PC solvent systems and MEC electrodes in b) DME, d) ACN, f) DMC and h) PC solvent systems. Rate capabilities of MIC electrodes in i) an anodic voltage range of $-2.5-0$ V and j) a cathodic voltage range of $0-2.5$ V. Rate capabilities of MEC electrodes in k) an anodic voltage range of $-2.5-0$ V and l) a cathodic voltage range of $0-2.5$ V.

pseudo-half-cell testing in the simple cell configuration without a reference electrode. The Mg ion storage behaviors of MIC and MEC were first investigated based on cyclic voltammetry (CV) in different electrolyte systems of DME, ACN, DMC, or PC containing 0.5 M magnesium bis(trifluoromethanesulfonyl) imide (Mg(TFSI)₂) (Figure 2 and Figures S6–S21, Supporting Information). The CV curves were characterized in the negative voltage range at different operating voltage windows between 0 and –0.6, –0.7, –0.8, and –2.5 V. This provided an insight into the voltage-dependent charge storage behaviors, particularly for MIC (Figure 2a,c,e,g). The CV curves of MIC in all of the tested solvent systems gradually decreased with increasing voltage window. This was attributed to the size of the primary solvation sheath, as EDL accumulation of larger charge carriers is very limited within the microporous structure mainly comprising <2 nm pores (Figure 2a,c,e,g).^[28–30] The highest capacitance values were observed in the CV curve of MIC in the ACN solvent, where substantial changes were observed with increasing operating voltage window (Figure 2c). This was attributed to the relatively small size of the ACN molecules, which resulted in a smaller solvation complex with Mg ions.^[30,31] Thus, charge carrier access into the internal narrow pores was easier in this system. However, diffusion of the Mg ion-ACN complex was impeded in the narrow pores, which led to the large distortion of the CV curves at lower voltages and poor rate performance (Figure 2c,i). Overall, these findings demonstrated that micropores are not suitable for capacitive Mg ion storage in organic solvent systems. The MEC served as an active electrode material with larger pores, where the CV curves in the negative voltage range was more rectangular-shaped and the capacitance values were higher (Figure 2b,d,f,h). The use of MEC in the DME solvent system led to the best rectangular shape with the voltage windows (Figure 2b), and the rate capability was far superior to those of the other solvent systems (Figure 2k). The capacitance values characterized in the different solvent systems converged to the same value at a lower scan rate, while the capacitance gap increased with scan rate (Figure 2k). This indicated that 1) the ultramicropores (≈2–5 nm) were key active site for capacitive Mg ion storage, 2) the specific capacitance of the Mg ions was not affected by the solvent type, and 3) the charge delivery rate of the Mg ion-solvent complex was significantly affected by the solvent system.

The cathodic CV curves were characterized in the positive voltage range between 0 and 0.6, 0.7, 0.8, and 2.5 V. Different capacitance values were obtained, despite using the same anion charge carrier, namely TFSI, in the different solvent systems (Figure 2j,l).^[16] This further demonstrated that the solvent systems strongly affect the charge storage behavior of the positively polarized electrode. More importantly, a wide stable operating voltage window was achieved, particularly in the DME solvent systems (Figure 2b). Within the significantly wide voltage windows between –2.5 and 2.5 V, the Mg ion-based charge carriers exhibited a highly stable and rapid charge delivery performance. This was closely related to the ionic interactions, which will be discussed in more detail in the following section.

To confirm the effectiveness of the pseudo-half-cell test results, a three-electrode-configuration test using the Ag/Ag⁺ reference electrode in a beaker cell was conducted for the Mg

ion storage behaviors of MEC in negative and positive voltage windows between –0.8 and –2.8 V and –0.8 and 1.2 V (Ag/Ag⁺), respectively, under DME solvent system (Figure S22, Supporting Information). In the three-electrode-configuration half-cell test, highly stable charge storage behaviors were obtained, which are the similar negative and positive CV curves to them of the pseudo-half-cell test results (Figure 2b). This reveals that the two-electrode-configuration using the excess MEC counter electrode can be an effective cell system to observe the Mg ion storage behaviors of MEC.

The multivalent cation effect was further evaluated based on comparisons with larger calcium ions and alkali cations (e.g., lithium and potassium ions) as charge carriers under the same conditions (Figure 3 and Figures S23–S34, Supporting Information). DME was selected as the solvent due to the previously observed high rate capabilities and wide voltage stability. Additionally, the 1st and 2nd CV curves of MEC in each electrolyte system were depicted in Figure S35, to support that there was no surface film formation reaction. The CV curve of the MICs with the Ca-ion-based electrolyte in the negative voltage range decreased with increasing voltage window (Figure 3a). Specifically, the capacitance of the MICs in the Ca ion-based electrolyte between –1.5 and 0 V was similar to that in the Mg ion-based electrolyte. However, the capacitance between –2.5 and –1.5 V was larger in the Ca ion system than the Mg ion system. Thus, Ca ion-DME complex physisorption was more favorable in narrow micropores despite the much larger ionic radius of Ca ions. Unlike the multivalent ion-based electrolyte systems, the alkali cation charge carriers in MICs lead to rectangular-shaped CV curves with higher capacitance values, even in the negative voltage ranges between –2.5 and 0 V (Figure 3c,e). This demonstrated that the Stokes radii of the alkali cations were smaller than those of the multivalent cations, thus the micropores fully accommodated the alkali cation-DME complexes. However, the capacitance between the multivalent ions and alkali ions was equalized when MEC was used as the active electrode material (Figure 3b,d,f,h), where the specific capacitance values converged at ≈105 F g^{–1} at a scan rate of 5 mV s^{–1}, regardless of cation type (Figure 3h). This indicated that EDL capacitance was not dependent on charge carrier type (e.g., ionic radius or oxidation number) at a given accessible active surface area.

The rate capabilities of the multivalent charge carriers were much higher than those of the alkali cations when both MIC and MEC were used (Figure 3g,h). Specifically, MEC operated at a high scan rate of 100 mV s^{–1} maintained ≈83% (87 F g^{–1}) and ≈74% (76 F g^{–1}) of the initial capacitance in the Mg and Ca ion-based electrolytes, respectively, while only ≈52% (53 F g^{–1}) and ≈47% (50 F g^{–1}) were maintained in the Li and K ion-based electrolytes. More importantly, the CV curves of the Ca, Li, and K ion systems in the positive voltage range exhibited severe oxidation behavior with increasing voltage range, particularly on the alkali cation systems, thereby limiting the stable voltage window. This irreversible oxidation reaction was caused by electrolyte decomposition with decreasing electron energy levels in the higher voltage region, where solvent oxidation can occur in a solvation complex with weaker ionic interaction between the salt and solvent molecules.

The first-principles DFT calculations reasonably support the experimentally observed behavior (Figure 4). Solvation free

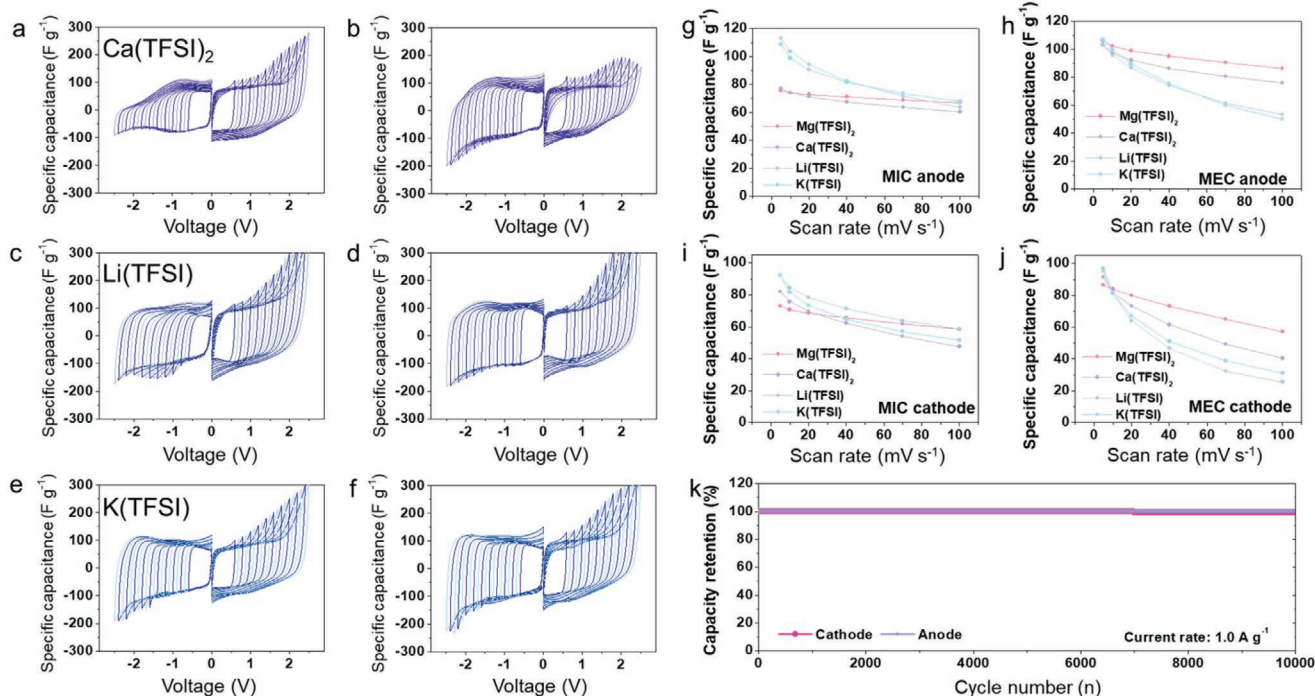


Figure 3. Capacitive charge storage behaviors of MIC and MEC electrodes under DME-based different electrolyte systems at different operating voltage windows. Cyclovoltammograms of MIC electrodes in 0.5 M a) Ca(TFSI)₂, c) Li(TFSI), and e) K(TFSI) electrolyte systems and MEC electrodes in b) Ca(TFSI)₂, d) Li(TFSI), and f) K(TFSI) electrolyte systems. Rate capabilities of MIC electrodes in g) an anodic voltage range of -2.5–0 V and i) a cathodic voltage range of 0–2.5 V. Rate capabilities of MEC electrodes in h) an anodic voltage range of -2.5–0 and j) a cathodic voltage range of 0–2.5 V. k) Cycling performances in the anodic and cathodic voltage ranges over 10000 cycles at a current density of 1 A g⁻¹.

energy ($\Delta G_{\text{solv.}}$) was calculated for the various pairs of cations (Mg²⁺, Ca²⁺, Li⁺, and K⁺) and solvents (DME, ACN, DMC, and PC) at defined coordination numbers (CN = 2, 4, and 6). Here, $\Delta G_{\text{solv.}}$ was defined as the stabilization energy of a gas-phase cation when forming a complex with a certain number of solvent molecules within the implicit solvation field of the corresponding solvent. A complex model was constructed for DME, where the cation forms a CN of 2 with one molecule^[32,33] and the remaining solvents to give a complex with as many solvent molecules as the CN. Regardless of the solvent type, the calculated $\Delta G_{\text{solv.}}$ values were the highest at a CN of 6 for Mg²⁺, Ca²⁺, and K⁺, and at a CN of 4 for Li⁺ due to its smaller ionic size and lower charge density (Figure S36a, Supporting Information). The optimized 6-coordination structures for Mg, Ca, and K were almost identical octahedral networks, and those of the 4-coordination structures for Li were tetrahedral networks (Figure S36b, Supporting Information). The solvation power of the various solvents increased with increasing dipole moment, namely 0.33, 1.46, 4.08, and 5.95 D for DMC, DME, ACN, and PC, respectively, and dielectric constant of the solvent molecules, namely 3.1, 7.2, 37.5, and 64.9 for DMC, DME, ACN, and PC, respectively. The magnitude and overall trends of the calculated $\Delta G_{\text{solv.}}$ values were similar to those of the experimental hydration free energy values of the cations. This confirmed that the calculation method was suitable for simulating the solvation environment (Table S1, Supporting Information).

Normalization of the stable solvation free energy values based on the number of molecules contributing to the complex generally indicated that DME had a significantly higher

contribution (Figure 4a). Thus, a DME solvent molecule had the strongest influence on the cations. Recent studies have shown that the redox stability of solvent molecules is affected by the molecular-level interactions within an electrochemical system, such as between the cations, anions, other solvent molecules, and the electrode surface.^[34–36] The ability to renormalize the highest occupied molecular orbital (HOMO) level of solvent molecules provides a good indication of oxidative stability. Interactions with anions destabilize the HOMO state, thereby promoting oxidation, while interactions with cations stabilize the HOMO state and hinder oxidation (Figure 4b). This primary effect dynamically determines the oxidation potential of solvent molecules. Specifically, oxidation potential is affected by changes in ion distribution and the complex structures at the electrode surface as a function of the applied potential.

Quantitative analysis was conducted by calculating the theoretical oxidation potential ($E_{\text{oxd.}}^{\circ}$), where a 1:1 interaction condition between each ion and solvent was assumed, thereby revealing the differences between the isolated solvent molecules (Figure 4c). For simplicity, $E_{\text{oxd.}}^{\circ}$ was calculated based on the single-point ionization and solvation energies of a complex structure optimized in the gas phase, where the repulsion between positively charged species upon oxidation was ignored. This provided an indication of the vertical oxidation potential (Figure S37, Supporting Information). The difference in the oxidation potentials ($\Delta E_{\text{oxd.}}^{\circ}$) due to the interaction with cations revealed large positive shifts in the order of Mg²⁺ > Ca²⁺ > Li⁺ > K⁺ at high solvation free energy values. Despite the differences

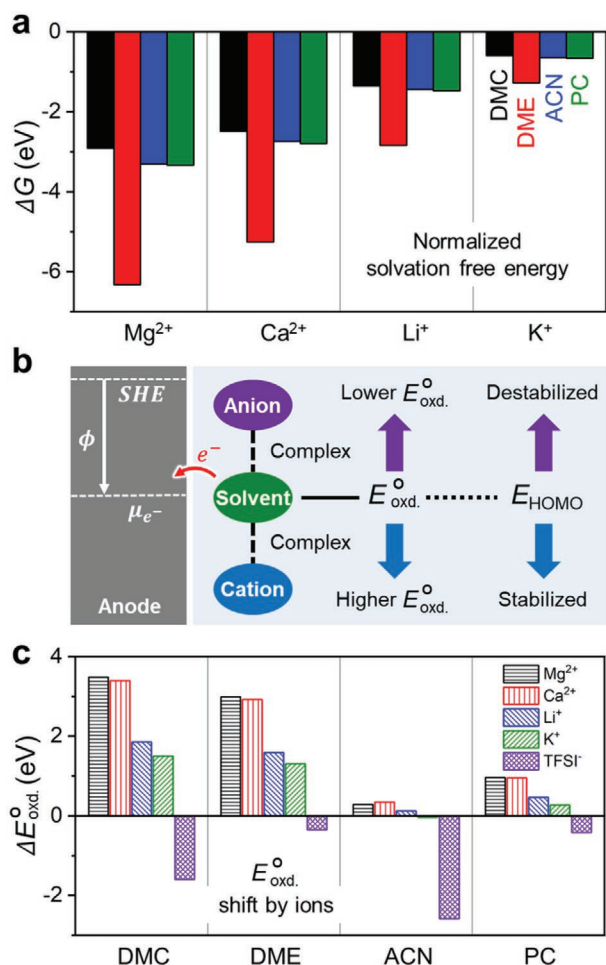


Figure 4. First principles calculation data obtained by a DFT method. a) Normalized solvation free energy of cations by the number of solvent molecules. b) Schematic illustration of the modulation of oxidation potential of a solvent molecule by complexation with ionic species. c) Oxidation potential shifts due to ion-solvent interactions.

between the solvents, the strong interactions with the divalent cations resulted in about double the potential shift compared to that of the monovalent cations. ΔE_{oxd}° is dependent on the complicated electronic structural changes that occur in the solvent molecules during oxidation due to ionic interactions. Thus, it is difficult to determine the detailed mechanism why DMC and DME show the highest cation effect. The complexes with anions exhibited a negative shift in ΔE_{oxd}° , where significant destabilization was observed in DMC and ACN. This ideal effect at an ion to solvent complex ratio of 1:1 leads to an ensemble result on the actual electrode surface depending on the number and structure of the cations, anions, and other solvent molecules surrounding the molecules. The modeling results provided an explanation for the experimentally observed dependence of oxidation stability on the nature of the solvent, where DMC and DME were more stable than other compounds due to the strong cation effect. In particular, the highest oxidative stability was achieved in DME due to two reasons. First, a small number of molecules contributed to the solvation shell, where the stabilization effect at a cation to solvent ratio of 1:1

was shared by three surrounding molecules rather than six molecules. Second, the anion effect was relatively weak compared to the other solvents. The experimental results according to the type of salt in DME can also be considered good for Mg^{2+} and Ca^{2+} , as these cations offered a stronger stabilizing effect than the others, even when the concentration of anions was twice that of monovalent cation salts.

Under the strong ionic interaction, a charge transfer reaction of the multivalent charge carriers stabilized by DME solvent molecules is highly limited by its neutralized charge state, thereby a pseudocapacitive reaction, which accompanies (partial) desolvation of the solvation complex, is obstructed despite the presence of redox-active functional groups on the surface of electrode. Quantitative contribution of the pseudocapacitive charge storage behaviors can be confirmed by CV tests in different operating voltage windows owing to the intrinsic differences between EDL capacitance and pseudocapacitance.^[24,37] Basically, EDL capacitance is not dependent on an operating voltage window, while pseudocapacitance is dependent on a specific redox-active voltage window because pseudocapacitance requires a relatively wide operating voltage window for activation. Accordingly, the CV curves with pseudocapacitive reactions show a capacitance increase with extending operating voltage ranges.^[37] This is contrast to that EDL-based charge storage manners show the similar capacitance values in all the operating voltage ranges. In the CV curves of MEC electrodes under the Mg ion-DME electrolyte system, as shown in Figure 2b, the CVs reveal the similar specific capacitance values in different operating voltage windows. This result reveals that the specific capacitance of MEC in the Mg ion-DME electrolyte system mainly originates from EDL-based charge storage behaviors.

Thus, the comparative experimental and theoretical calculation results indicated that the smaller multivalent cation-DME complex delivered more charges over a wide voltage range and at a higher rate, particularly when the smaller multivalent Mg ion was used as a charge carrier (Figures 3 and 4). Further, the capacitive charge storage behaviors of MECs in the Mg ion-DME electrolyte system exhibited highly stable cycling performance over 10000 cycles in both negative and positive voltage windows. Specifically, the capacitance retention was nearly 100% after 10000 consecutive cycles, thereby demonstrating the great potential for high-performance Mg ion supercapacitors (Figure 3k).

High-performance Mg ion supercapacitors were assembled in a symmetric configuration using two MEC electrodes with the same mass loading contents of $\approx 1 \text{ mg cm}^{-2}$ in a high-performance electrolyte system of 0.5 M $Mg(TFSI)_2$ in DME. The energy and power balances between the negative and positive electrodes were adjusted based on galvanostatic charge/discharge testing in different voltage ranges (e.g., -2.0 to 0 V and 0 to 2.0 V vs SHE) in a half cell configuration with a Ag/Ag^+ reference electrode and Pt counter electrode at different current rates. The negative and positive electrodes exhibited similar rate capabilities within a current density range of 0.2 to 1.5 $A g^{-1}$, where a capacitance gap of $\approx 15\%$ was observed (Figure 5a). The negative electrode delivered a specific capacitance of $\approx 115 \text{ F g}^{-1}$ at 0.2 $A g^{-1}$, which was gradually decreased with current density to ≈ 105 , ≈ 98 , ≈ 94 , ≈ 90 , and $\approx 85 \text{ F g}^{-1}$ at 0.3, 0.5, 0.7, 1.0, and 1.5 $A g^{-1}$, respectively (Figure 5a). Further, the positive electrode delivered a specific capacitance of ≈ 97 , ≈ 90 , ≈ 84 , ≈ 80 , ≈ 78 ,

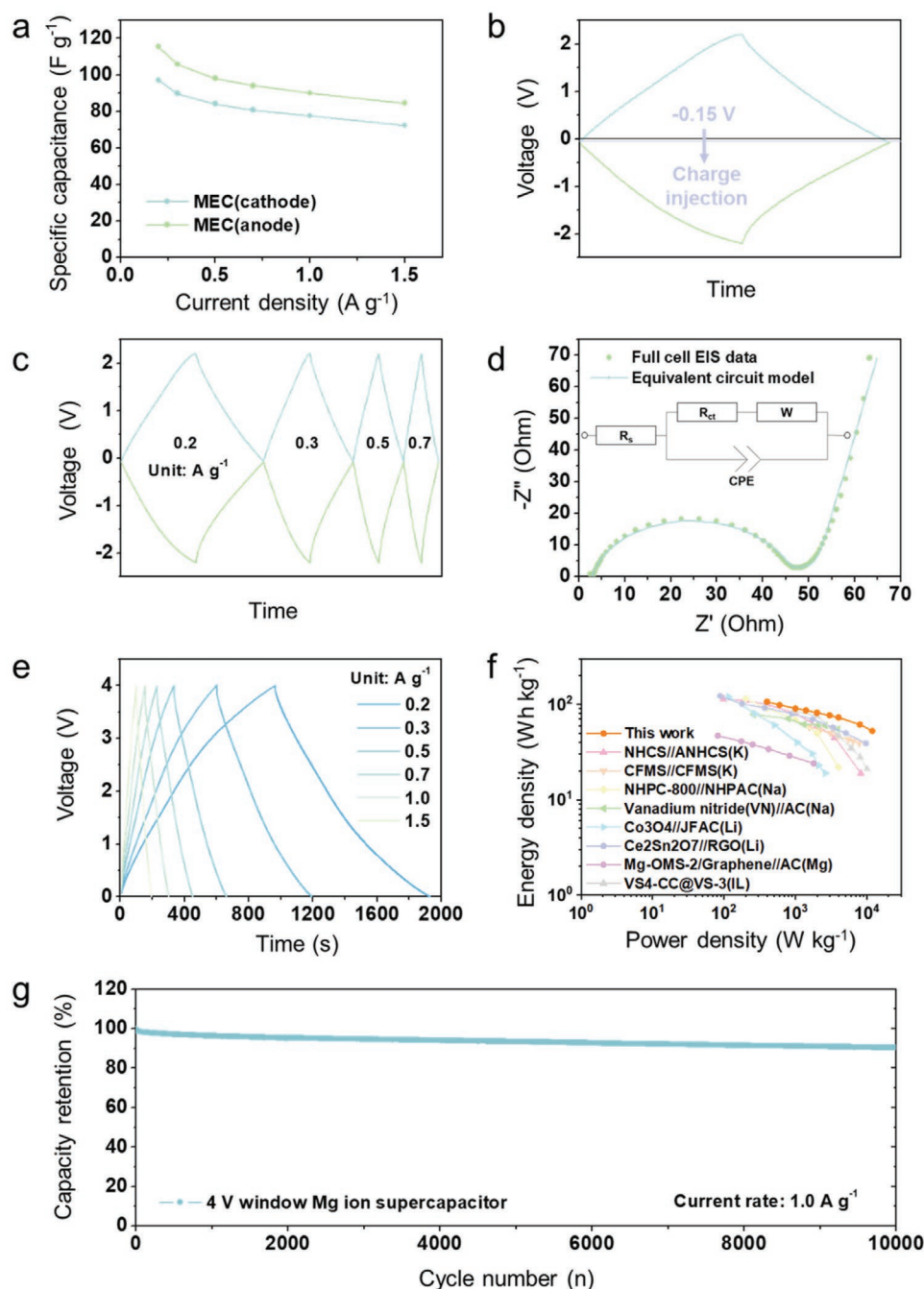


Figure 5. Electrochemical performances of MEC electrodes at different voltage ranges and Mg ion supercapacitors based on a symmetric MEC electrode pair over a voltage window of 4 V, in an electrolyte of 0.5 m $\text{Mg}(\text{TFSI})_2$ in DME. a) Rate capabilities of MEC electrodes in an anodic and cathodic voltage ranges of -2.0 – 0 and 0 – 2.0 V, respectively, at different current rate. b) Galvanostatic charge/discharge curves of MEC-based anode and cathode of which capacities were tuned by a charge injection to adjust energy balance of the electrode pair. c) Galvanostatic charge/discharge curves of the charge-injected MEC-based anode and cathode at different current rates. d) EIS profiles and e) galvanostatic charge/discharge curves at different current rates of the Mg ion supercapacitors. f) Ragone plots of several energy storage devices including the Mg ion supercapacitors. g) Cycling performances of the Mg ion supercapacitors over 10000 cycles at a current rate of 1.0 A g^{-1} .

and $\approx 72 \text{ F g}^{-1}$ at 0.2, 0.3, 0.5, 0.7, 1.0, and 1.5 A g^{-1} , respectively (Figure 5a). The energy balance was tuned by controlling the operating voltage windows of both electrodes via charge injection, where an optimal onset potential of -0.15 V was chosen (Figure 5b).^[38] The charge-injected electrodes exhibited similar

capacitance values at different current densities, thereby demonstrating their good energy and power balance (Figure 5c).

The charge-injected MEC electrodes were used to assemble a 4 V-window Mg ion supercapacitor with a symmetric configuration using a 2032-type coin cell. Electrochemical impedance

spectroscopy (EIS) and galvanostatic charge/discharge testing was conducted at various current densities (Figure 4d,e). The EIS profile exhibited a typical Nyquist plot for supercapacitors, which included solution resistance, charge transfer resistance, and Warburg impedance, as illustrated by the inset equivalent circuit model in Figure 5d. The electrochemical series resistance value was $\approx 50 \Omega$ (Figure 5d), and the specific single electrode capacitance of the Mg ion supercapacitors was 96, 89, 82, 78, 74, and $70 \text{ F g}_{\text{electrode}}^{-1}$ at 0.2, 0.3, 0.5, 0.7, 1.0, and 1.5 A g^{-1} . The device capacitance is a quarter of the respective single electrode capacitance values which correspond to specific capacities of 53, 49, 45, 43, 41, and $38 \text{ mA h g}_{\text{electrode}}^{-1}$, respectively. The average voltage of the galvanostatic profiles was relatively consistent at $\approx 2 \text{ V}$ within the current density range of 0.2 to 1.5 A g^{-1} . Accordingly, the calculated specific energy and power densities were $\approx 106 \text{ W h kg}^{-1}$ and $\approx 11870 \text{ W kg}^{-1}$, respectively.

The energy and power relationship was depicted as a Ragone plot and compared with previously reported high-performance supercapacitors (Figure 4f).^[39–46] The MEC-based Mg ion supercapacitors offered at least double the specific energy density and over four times the specific power density offered by previously reported Mg ion supercapacitors. In addition, this multivalent ion supercapacitor exceeded the energy and power capabilities of all other alkali ion-based supercapacitors reviewed in the comparison. The MEC-based Mg ion supercapacitors also exhibited a highly stable cycling performance with $>90\%$ capacitance retention over 10000 repeated galvanostatic charge/discharge cycles at 1.0 A g^{-1} (Figure 5g). After the long-term cycling process over 10000 cycles, the EIS profile of the Mg ion supercapacitors shows the similar semicircle to that of the initial cycle (Figure S38, Supporting Information). In addition, the electrochemical series resistance value after 10000 cycles is $\approx 55 \Omega$, which is $\approx 10\%$ higher value than that of the initial one. This result supports the great cycling stability of the MEC-based Mg ion supercapacitors. Thus, E_{oxd}^0 of DME solvent is significantly increased by the chelate effect of three surrounding DME molecules with twice CNs and the stronger interactions between the smaller divalent Mg ion and DME, resulting in the wide operating voltage window of 4 V. In contrast, other electrolyte systems such as Ca, Li, and K ion-DME complexes did not show the stable voltage window (Figure S39, Supporting Information). These 4 V window Mg ion supercapacitors show great potential as multivalent supercapacitors, which could be a feasible candidate for commercial applications in the light of that the organic electrolyte system is much cheaper than ionic liquid-based electrolyte systems. Further evaluation is recommended, particularly regarding the relationships between the multivalent charge carriers, pore structures, and solvent systems. It is expected that continued research allows of the development of higher performing multivalent supercapacitors. Additionally, this result for the Mg ion charge carrier-DME system with the wide operating voltage window could provide an insight in the fields of rechargeable Mg ion batteries and Mg ion hybrid capacitors.

3. Conclusion

In summary, the capacitive multivalent ion storage behavior on nanoporous carbons was investigated within various solvents,

such as ACN, DMC, DME, and PC. These observations were compared to alkali ion storage behavior under the same conditions. When MIC was used as the electrode material, the Mg ion-organic solvent complexes exhibited voltage-dependent cyclovoltammograms with poor capacitance. However, nearly rectangular-shaped cyclovoltammograms are observed when MEC was used in all of the solvent systems. This demonstrated that ultramesopores are more suitable for multivalent solvation complexes. The specific capacitance for the Mg ion charge carrier was not affected by solvent type, while the rate capability of the Mg ion-solvent complex was significantly affected. Overall, the Mg ion-DME pair offered the highest rate capability. A key finding of the systematic electrochemical testing in the Mg, Ca, K, Li ion-DME electrolyte systems was a wide stable operating voltage window between -2.5 – 2.5 V for the Mg ion-DME system. The DFT calculations indicated that DME was associated with fewer molecules participating in the solvation shell, and was shared by three surrounding molecules instead of six molecules. Thus, the strongest stabilization effect was achieved under a cation to solvent ratio of 1:1. The strong ionic interactions allowed for the Mg ion supercapacitors to deliver a high specific energy and power of 106 Wh kg^{-1} and 11870 W kg^{-1} , respectively, within the wide operating voltage window of 4 V.

4. Experimental Section

Preparation of MIC and MEC Electrodes: Polyaniline precursors were synthesized via a previously reported procedure. In the fabrication process, aniline monomer (2 mmol, DC Chemical, Korea) and oxalic acid (0.5 mmol, Sigma-Aldrich) were dissolved in distilled water using a 30 min ultrasound treatment. Subsequently, ammonium persulfate (2 mmol, Daejung Co. Ltd., Korea) which was precooled to $4 \text{ }^\circ\text{C}$ was added into the reactor with stirring. After the mixture was left for 20 h at $4 \text{ }^\circ\text{C}$, the product materials were washed several times with distilled water and methanol, then vacuum-dried at $80 \text{ }^\circ\text{C}$ for 24 h. The resulting polyaniline precursors were heated with KOH (weight ratios of 100%, and 300% to polyaniline) to $800 \text{ }^\circ\text{C}$ under nitrogen flow of $\approx 200 \text{ mL min}^{-1}$. A heating rate of $10 \text{ }^\circ\text{C min}^{-1}$ was applied and the final temperature was held for 2 h. When a weight ratio of 300 wt% KOH to polyaniline was used for the sample preparation, the targeted MEC samples were prepared, while another sample, MICs, were prepared with the heating process with 100% KOH. The resulting products were washed with distilled water and methanol several times and stored in a vacuum oven at $30 \text{ }^\circ\text{C}$.

Characterization: Pore structure of MICs and MECs was analyzed by a nitrogen adsorption and desorption isotherm method at $-196 \text{ }^\circ\text{C}$. Specific surface area and pore size distribution were calculated by BET and Barret–Joyner–Halenda methods, respectively. Carbon microstructures of MICs and MECs were characterized by Raman spectroscopy using a Renishaw InVia Raman spectrometer (Renishaw, UK) equipped with a laser with a wavelength of 514 nm, 0.15 mW output, and 1200 groove/mm grating. The spot size of the laser was focused through a $100\times$ optical lens, and the exposure time was set to 10 s. XRD (Rigaku, DMAX 2500) was performed using a $\text{Cu-K}\alpha$ radiation ($\lambda = 1.54 \text{ \AA}$) at 40 kV and 100 mA with a range of 5 – $60^\circ 2\theta$. Carbon local microstructure and morphologies were observed by FE-TEM (JEM2100F, JEOL, Japan) and FE-SEM (S-4300SE, Hitachi, Japan). The chemical surface properties of the samples were measured by XPS (PHI 5700 ESCA, Chanhassen, USA) using monochromatic $\text{Al-K}\alpha$ radiation.

Electrochemical Characterization: Charge storage behaviors of the MIC and MEC electrodes under different electrolyte systems were analyzed by CV tests at different voltage windows and different scan rates (PGSTAT302N, Metrohm Autolab, Utrecht, The Netherlands)

using a 2032-type coin cell. Excess MECs corresponding to counter to active electrode capacity ratio (mass ratio) of ≈ 20 were used as counter electrode. Different electrolyte systems of 0.5 M Mg(TFSI)₂, Ca(TFSI)₂, LiTFSI, or KTFSI dissolved in ACN, DMC, DME, or PC were used for the electrochemical tests. A glass microfiber filter was used as a separator (GF/F, Whatman). The working electrodes were prepared by mixing the active material (90 wt%) and polyvinylidene fluoride (10 wt%) in N-methyl-2-pyrrolidone. The resulting slurries were applied uniformly to Al foil. The electrode was dried at 120 °C for 2 h and roll pressed; the average active material loading was ≈ 1 mg cm⁻². For the symmetric supercapacitors, galvanostatic charge/discharge methods were used at different current rates and different operating voltage windows, and EIS tests were conducted in a frequency range of 1 mHz to 0.1 MHz using an impedance analyzer (ZIVE SP2, WonATech). The specific capacitance of the Mg ion supercapacitors was calculated by using the formula:

$$C_{\text{carbon}} = \frac{4I_{\text{cons}}}{m dV/dt} \quad (2)$$

where, I is the constant current and m is the total mass for both carbon electrodes, and dV/dt was calculated from the slope obtained by fitting a straight line to the discharge curve.

Computational Methods: Quantum mechanical calculations based on DFT were carried out using the Schrodinger Jaguar suite v. 10.9.^[47] The Pople-type 6-31G**++ basis-set^[48] and B3LYP exchange-correlation functional^[49,50] were selected. Solvation effects were evaluated using polarizable continuum model method as implemented in the Jaguar package with experimental dielectric constant (ϵ) and approximated probe radii (R) from the molecular weight and liquid density of each solvent ($\epsilon = 3.1, 7.2, 37.5,$ and 64.9 ; $R = 2.56, 2.74, 2.19,$ and 2.56 Å for DMC, DME, ACN, and PC, respectively).

Supporting Information

Supporting Information is available from the Wiley Online Library or from the author.

Acknowledgements

This research was supported by the Basic Science Research Program through the National Research Foundation of Korea (NRF) funded by the Ministry of Education (NRF-2019R1A2C1084836, NRF-2021M3H4A1A01079367, NRF-2020M3H4A1A0308425612, and NRF-2021R1A4A2001403).

Conflict of Interest

The authors declare no conflict of interest.

Data Availability Statement

Research data are not shared.

Keywords

electrodes, magnesium ions, multivalent ions, nanoporous carbon, supercapacitors

Received: April 2, 2021

Revised: June 7, 2021

Published online:

- [1] P. Simon, Y. Gogotsi, *Nat. Mater.* **2020**, *19*, 1151.
- [2] A. C. Forse, J. M. Griffin, C. Merlet, J. Carretero-Gonzalez, A. R. O. Raji, N. M. Trease, C. P. Grey, *Nat. Energy* **2017**, *2*, 16216.
- [3] M. Salanne, B. Rotenberg, K. Naoi, K. Kaneko, P. L. Taberna, C. P. Grey, B. Dunn, P. Simon, *Nat. Energy* **2016**, *1*, 16070.
- [4] H. Kim, W. Choi, J. Yoon, J. H. Um, W. Lee, J. Kim, J. Cabana, W. S. Yoon, *Chem. Rev.* **2020**, *120*, 6934.
- [5] K. Breitsprecher, M. Janssen, P. Srimuk, B. L. Mehdi, V. Presser, C. Holm, S. Kondrat, *Nat. Commun.* **2020**, *11*, 6085.
- [6] M. R. Lukatskaya, B. Dunn, Y. Gogotsi, *Nat. Commun.* **2016**, *7*, 12647.
- [7] Y. Zhai, Y. Dou, D. Zhao, P. F. Fulvio, R. T. Mayes, S. Dai, *Adv. Mater.* **2011**, *23*, 4828.
- [8] H. Shao, Y. C. Wu, Z. Lin, P. L. Taberna, P. Simon, *Chem. Soc. Rev.* **2020**, *49*, 3005.
- [9] C. Prehal, C. Koczwar, N. Jäckel, A. Schreiber, M. Burian, H. Amenitsch, M. A. Hartmann, V. Presser, O. Paris, *Nat. Energy* **2017**, *2*, 16215.
- [10] R. Futamura, T. Iiyama, Y. Takasaki, Y. Gogotsi, M. J. Biggs, M. Salanne, J. Ségalini, P. Simon, K. Kaneko, *Nat. Mater.* **2017**, *16*, 1225.
- [11] C. Merlet, B. Rotenberg, P. A. Madden, P.-L. Taberna, P. Simon, Y. Gogotsi, M. Salanne, *Nat. Mater.* **2012**, *11*, 306.
- [12] A. C. Forse, C. Merlet, J. M. Griffin, C. P. Grey, *J. Am. Chem. Soc.* **2016**, *138*, 5731.
- [13] C. Merlet, C. Pean, B. Rotenberg, P. A. Madden, B. Daffos, P. L. Taberna, P. Simon, M. Salanne, *Nat. Commun.* **2013**, *4*, 2701.
- [14] J. Huang, B. G. Sumpter, V. Meunier, *Angew. Chem., Int. Ed.* **2008**, *47*, 520.
- [15] H. Wang, A. C. Forse, J. M. Griffin, N. M. Trease, L. Trognon, P. L. Taberna, P. Simon, C. P. Grey, *J. Am. Chem. Soc.* **2013**, *135*, 18968.
- [16] J. M. Griffin, A. C. Forse, W. Y. Tsai, P. L. Taberna, P. Simon, C. P. Grey, *Nat. Mater.* **2015**, *14*, 812.
- [17] C. Pean, B. Daffos, B. Rotenberg, P. Levitz, M. Haefele, P.-L. Taberna, P. Simon, M. Salanne, *J. Am. Chem. Soc.* **2015**, *137*, 12627.
- [18] L. Zhang, X. Yang, F. Zhang, G. Long, T. Zhang, K. Leng, Y. Zhang, Y. Huang, Y. Ma, M. Zhang, Y. Chen, *J. Am. Chem. Soc.* **2013**, *135*, 5921.
- [19] Z. Li, X. Mu, Z. Zhao-Karger, T. Diemant, R. J. Behm, C. Kubel, M. Fichtner, *Nat. Commun.* **2018**, *9*, 5115.
- [20] H. Tian, T. Gao, X. Li, X. Wang, C. Luo, X. Fan, C. Yang, L. Suo, Z. Ma, W. Han, C. Wang, *Nat. Commun.* **2017**, *8*, 14083.
- [21] S. Woo, P. W. K. Rothmund, *Nat. Commun.* **2014**, *5*, 4889.
- [22] S. Kondrat, A. Kornyshev, *J. Phys.: Condens. Matter* **2013**, *25*, 119501.
- [23] M. Li, J. Lu, X. Ji, Y. Li, Y. Shao, Z. Chen, C. Zhong, K. Amine, *Nat. Rev. Mater.* **2020**, *5*, 276.
- [24] S. Moon, D. -H. Kim, J. H. Kwak, S. M. Lee, H.-D. Lim, K. Kang, H. -J. Jin, Y. S. Yun, *Appl. Surf. Sci.* **2021**, *537*, 148037.
- [25] J.-B. Wu, X. Zhang, M. Ijäs, W.-P. Han, X.-F. Qiao, X.-L. Li, D.-S. Jiang, A. C. Ferrari, P.-H. Tan, *Nat. Commun.* **2014**, *5*, 5309.
- [26] S. Y. Cho, Y. S. Yun, D. Jang, J. W. Jeon, B. H. Kim, S. Lee, H.-J. Jin, *Nat. Commun.* **2017**, *8*, 74.
- [27] A. C. Ferrari, D. M. Basko, *Nat. Nanotechnol.* **2013**, *8*, 235.
- [28] K. Zou, P. Cai, B. Wang, C. Liu, J. Li, T. Qiu, G. Zou, H. Hou, X. Ji, *Nano-Micro Lett.* **2020**, *12*, 121.
- [29] H. W. Kwak, M. E. Lee, H.-J. Jin, Y. S. Yun, *J. Power Sources* **2019**, *418*, 218.
- [30] H. M. Joseph, M. Fichtner, A. R. Munnangi, *J. Energy Chem.* **2021**, *59*, 242.
- [31] T. J. Seguin, N. T. Hahn, K. R. Zavadil, K. A. Persson, *Front. Chem.* **2019**, *7*, 175.
- [32] A. K. Lautar, J. Bitenc, T. Rejec, R. Dominko, J.-S. Filhol, M.-L. Doublet, *J. Am. Chem. Soc.* **2020**, *142*, 5146.

- [33] Y. Chen, N. R. Jaegers, H. Wang, K. S. Han, J. Z. Hu, K. T. Mueller, V. Murugesan, *J. Phys. Chem. Lett.* **2020**, *11*, 6443.
- [34] A. Baskin, D. Prendergast, *J. Phys. Chem. Lett.* **2019**, *10*, 4920.
- [35] O. Borodin, X. Ren, J. Vatamanu, A. von Wald Cresce, J. Knap, K. Xu, *Acc. Chem. Res.* **2017**, *50*, 2886.
- [36] O. Borodin, W. Behl, T. R. Jow, *J. Phys. Chem. C* **2013**, *117*, 8661.
- [37] J. K. Han, M. E. Lee, H. J. Choi, H.-J. Jin, Y. S. Yun, *Electrochim. Acta* **2019**, *302*, 71.
- [38] N. R. Kim, S. M. Lee, M. W. Kim, H. J. Yoon, W. G. Hong, H. J. Kim, H. J. Choi, H.-J. Jin, Y. S. Yun, *Adv. Energy Mater.* **2017**, *7*, 1700629.
- [39] D. Qiu, J. Guan, M. Li, C. Kang, J. Wei, Y. Li, Z. Xie, F. Wang, R. Yang, *Adv. Funct. Mater.* **2019**, *29*, 1903496.
- [40] Y. Feng, S. Chen, J. Wang, B. Lu, *J. Energy Chem.* **2020**, *43*, 129.
- [41] S. Wei, C. Wang, S. Chen, P. Zhang, K. Zhu, C. Wu, P. Song, W. Wen, L. Song, *Adv. Energy Mater.* **2020**, *10*, 1903712.
- [42] K. Zou, P. Cai, C. Liu, J. Li, X. Gao, L. Xu, G. Zou, H. Hou, Z. Liu, X. Ji, *J. Mater. Chem. A* **2019**, *7*, 13540.
- [43] P. Sennu, S. Madhavi, V. Aravindan, Y. -S. Lee, *ACS Nano* **2020**, *14*, 10648.
- [44] Q. Wu, Y. Liu, H. Wang, J. Hou, Y. Li, Q. Duan, *J. Mater. Chem. A* **2020**, *8*, 5517.
- [45] M. Ramu, J. R. Chellan, N. Goli, P. Joaquim, V. Cristobal, B. C. Kim, *Adv. Funct. Mater.* **2020**, *30*, 1906586.
- [46] H. Zhang, K. Ye, K. Zhu, R. Cang, X. Wang, G. Wang, D. Cao, *ACS Sustainable Chem. Eng.* **2017**, *5*, 6727.
- [47] A. D. Bochevarov, E. Harder, T. F. Hughes, J. R. Greenwood, D. A. Braden, D. M. Philipp, D. Rinaldo, M. D. Halls, J. Zhang, R. A. Friesner, *Int. J. Quantum Chem.* **2013**, *113*, 2110.
- [48] P. C. Hariharan, J. A. Pople, *Chem. Phys. Lett.* **1972**, *66*, 217.
- [49] A. D. Becke, *J. Chem. Phys.* **1993**, *98*, 5648.
- [50] C. Lee, W. Yang, R. G. Parr, *Phys. Rev. B* **1988**, *37*, 785.